J Math Imaging Vis (2007) 28: 81–97
DOI 10.1007/s10851-007-0015-8

Texture-Oriented Anisotropic Filtering and Geodesic Active Contours in Breast Tumor Ultrasound Segmentation

Miguel Alemán-Flores · Luis Álvarez · Vicent Caselles

Published online: 9 June 2007

Abstract In this paper we present an anisotropic filter for speckle reduction in ultrasound images and an adaptation of the geodesic active contours technique for the segmentation of breast tumors. The anisotropic diffusion we propose is based on a texture description provided by a set of Gabor filters and allows reducing speckle noise while preserving edges. Furthermore, it is used to extract an initial presegmentation of breast tumors which is used as initialization for the active contours technique. This technique has been adapted to the characteristics of ultrasonography by adding certain texture-related terms which provide a better discrimination of the regions inside and outside the nodules. These terms allow obtaining a more accurate contour when the gradients are not high and uniform.

Keywords Ultrasound · Breast cancer · Segmentation · Active contours · Anisotropic filtering

1 Introduction

Early diagnosis is a crucial factor in breast cancer treatment, and medical imaging is a very powerful assessment tool. The two main types of images used in this kind of diagnosis are mammography and ultrasonography. In this work, we have focussed on the latter, for which a series of criteria has been described to distinguish benign from malignant lesions. These criteria include hyperechogenicity (the nodule is brighter in the ultrasound image than the surrounding breast fat), ellipsoid shape, two or three gentle lobulations (lobes which form the tumor) and thin echogenic capsule as benignity criteria. On the other hand, hypoechogenicity (the nodule is darker in the ultrasound image than the surrounding breast fat), acoustic shadowing (attenuation of sound behind all or part of the nodule, which appears as a darker region under the lesion), ramifications, microlobulations (small rounded projections), angular margins, spiculation (alternating hypoechoic and relatively hyperechoic straight lines radiating out perpendicular from surface of the nodule), calcifications (punctate bright spots within a solid nodule) and taller-than-wide shape are considered as malignancy findings [36]. In a computer-aided system, the accurate segmentation of breast nodules in ultrasonography is a major task for a further analysis of the global shape and local contour variations of the tumor, on which most criteria are based. However, this task implies many problems when automation is intended, since the presence of speckle noise and shadows, the low or non-uniform contrast of certain structures, and the variability of the echogenicity of the nodules make it very difficult to obtain a segmentation which can be useful for the diagnosis. This explains the fact that most of the results regarding the semiautomatic segmentation and characterization of breast tumors have been limited so far [11, 12, 22, 26].

There are many different approaches for the segmentation of breast nodules. Manual delimitation is time-consuming, tedious and with a considerable inter- and intra-observer variability. On the other hand, fully automatic

M. Alemán-Flores (✉) · L. Álvarez
Departamento de Informática y Sistemas, Universidad de Las Palmas de Gran Canaria, 35017, Las Palmas, Spain
e-mail: maleman@dis.ulpgc.es

L. Álvarez
e-mail: lalvarez@dis.ulpgc.es

V. Caselles
Departament de Tecnologia, Universitat Pompeu Fabra, 08003, Barcelona, Spain
e-mail: vicent.caselles@upf.edu

methods require *a priori* knowledge of the shape of the nodule, which is not usually available. Between both extremes, we can find semiautomatic methods, which provide good results by means of a reduced interaction with the user.

We propose a combination of different techniques to extract a semiautomatic segmentation of breast nodules. Firstly, an anisotropic texture-guided diffusion is used to reduce speckle. Secondly, a front propagation algorithm is applied to obtain a pre-segmentation of the nodule. This algorithm starts from an inner point selected by the specialist, which is the only interaction required to the user. Finally, in order to refine the pre-segmentation, we use an adaptation of the geodesic active regions technique (combined with the classical geodesic active contour term) designed to tackle the particularities of ultrasound images. In this paper, we use known techniques, such as anisotropic diffusion, balloon methods, Gabor filters or geodesic active contours. We combine and refine such techniques with the purpose of ultrasound image segmentation. In particular, we propose an anisotropic texture-guided diffusion and a region based geodesic active contour using the response of a set of Gabor filters.

In the anisotropic diffusion step, we adapt the ideas of the classical Perona-Malik equation [31] to the diffusion of ultrasound images. For that, we use a set of texture descriptors $\mathbf{R}$ based on Gabor filters and we inhibit the diffusion across changes in these descriptors (determined by large values of the modulus of the gradient of $\mathbf{R}$). This filtering will permit us to obtain a more precise pre-segmentation. The pre-segmentation is computed with a front propagation scheme with a speed depending (inversely) on the modulus of the gradient, which is analogous to the inflation force used in [13]. These balloon forces have traditionally been included in the level set formulation [29] of active contours [4–6, 23, 28], but they are used here as a pre-processing step to get an initial segmentation as close as possible to the contour of the nodule. In the last step, in order to improve the final segmentation, we use a combination of the geodesic edge based and region based active contours; the region descriptors being based on the responses of a set of Gabor filters at several orientations and scales. We explore a local variant of the model proposed in [8, 34, 35] and we introduce a new variant of it, we test both of them for our set of images. Many variants of active contours [4–6, 13, 21, 23, 28] have previously been applied to the segmentation of medical images [10, 20], textured regions [2, 8, 30, 32, 34, 35], and other situations whose conditions are similar to ours. In particular, the works [8, 9, 15, 30, 34, 35] have also used region descriptors or statistical information and the last two ones have used the responses of Gabor filters as texture descriptors. Finally, let us mention that novel level set methods for image segmentation include motion-based level set segmentation [14], segmentation of natural textures [19] and ultrasound segmentation with non-parametric intensity and shape models [33].

The rest of the paper is structured as follows: Sect. 2 explains the texture-based anisotropic filtering process which allows reducing speckle. Section 3 shows the extraction of a pre-segmentation by means of a front propagation scheme. In Sect. 4, we review the basic region based active contours for scalar and vector features and we propose some extensions. In particular, we describe a region based active contour model based on a set of Gabor filter responses used as texture descriptors. Section 5 presents some results and comparisons. Finally, in Sect. 6, we give an account of our main conclusions.

2 Speckle Reducing Anisotropic Diffusion Based on Vector Descriptors

Ultrasound images present highly disturbing speckle noise. Moreover, in many cases, the low contrast between the structures to be segmented and the background, as well as the shadows which may appear depending on the properties of the tissues, make it even harder to locate the edges of the different elements. Figure 1 shows an example of a breast nodule which is very hard to process, since it combines rounded and angular margins, and present diffuse edges, prolongations, concavities and non-uniform intensity. It is necessary to remove speckle before dealing with the problem of segmentation. Classical speckle removing filters include local statistics and minimum square error schemes [17, 25, 27]. Truncated median [16] has proved very useful in the reduction of speckle using an iterative algorithm to approximate the mode using small windows. Isotropic diffusion

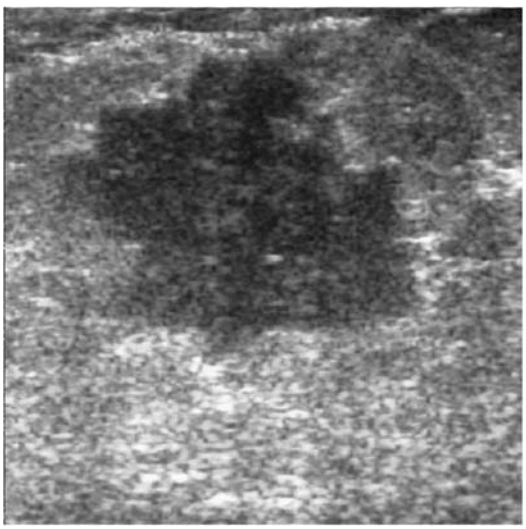

Fig. 1 Original ultrasound image of a breast nodule with rounded and angular margins, diffuse edges, prolongations, concavities and non-uniform intensity

is not suitable since it should be strong enough to reduce speckle but low enough to preserve edges. On the other hand, anisotropic diffusion tries to reduce the noise of the images preserving the contrast of the edges, in such a way that the contours of the objects in the scene are not altered by the diffusion process (see [37] for more details). In this paper $\Omega \subset \mathbb{R}^2$ denotes the image domain which we assume to be a rectangle in $\mathbb{R}^2$ and $I_0 : \Omega \to \mathbb{R}$ denotes a given image. A typical anisotropic filter applied to I_0 is given by the solution $I(t, x, y)$, $t > 0$, $(x, y) \in \Omega$, of Perona–Malik equation [31]:

$$\begin{aligned} \frac{\partial I}{\partial t} &= \operatorname{div}(c(\|\nabla I\|)\nabla I) \\ I(t = 0) &= I_0 \end{aligned} \tag{1}$$

with Neumann boundary conditions, i.e., $\nabla I \cdot \nu^{\Omega} = 0$ where ν^{Ω} denotes the outer unit normal to the boundary of Ω.

In this equation, $c(r)$ is a monotonic decreasing function of $r > 0$, such as, for example:

$$c(r) = e^{-(\frac{r}{k})^2}, \tag{2}$$

where k is a constant which determines the contrast of the edges to preserve.

This kind of filters works properly in many kinds of images, mainly when the objects are defined by uniform intensity regions. However, in our case, the textures of the regions make it necessary to express the similarity between different areas in terms of texture descriptors, instead of intensities. Speckle reducing anisotropic diffusion has previously been introduced, mostly in synthetic aperture radar images [38]. We propose to use Gabor filters [18] to characterize the textures, and the gradient of the filtered images as a texture-based edge detector. A Gabor filter whose scale and horizontal and vertical frequencies are given by $\sigma > 0$, k_x and k_y in $\mathbb{R}$, respectively, can be expressed as:

$$G^{\sigma}_{k_x,k_y}(x, y) = e^{-\frac{x^2+y^2}{2\sigma^2}}(\cos(k_x x + k_y y)). \tag{3}$$

We use a set of S scales, N frequencies within each scale, and two orientations (horizontal and vertical) for each frequency. Fixed a certain scale $\sigma_0 > 0$ and a certain frequency $k_0 > 0$, the outputs of the filters are calculated as the convolution:

$$F^{s}_{n_x,n_y} = I * G^{s\sigma_0}_{n_x k_0, n_y k_0}, \tag{4}$$

where $1 \le s \le S$, $-N \le n_x \le N$ and $0 \le n_y \le N$.

These filters combine orientation and frequency and provide a description of the distribution of the intensities in the region where they are applied (see Fig. 2). Due to the high variability in the aspect of the different tumors, it is difficult to establish a certain pattern in the response of the filters which allows identifying all of them.

Taking the Perona–Malik equation (1) as a model, we propose to penalize the diffusion along high texture gradients. If $\mathbf{R}(x, y)$ denotes the vector formed by the responses of a family of Gabor filters applied to the image $I(0)$ at point (x, y), we use the following anisotropic diffusion equation:

$$\frac{\partial I}{\partial t} = \operatorname{div}(c(\|\nabla \mathbf{R}\|)\nabla I), \tag{5}$$

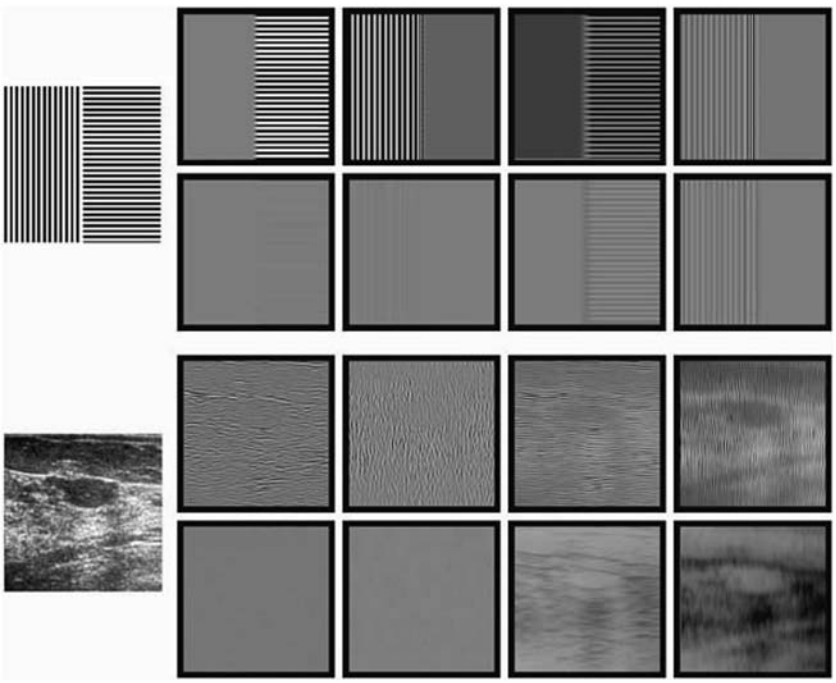

Fig. 2 Example of the application of 8 Gabor filters to a synthetic textured image representing well defined oscillations and an ultrasound image. For each of the images: *Top row*: $\sigma = 5$, $k_x = 7$, $k_y = 0$; $\sigma = 5$, $k_x = 0$, $k_y = 7$; $\sigma = 10$, $k_x = 7$, $k_y = 0$; $\sigma = 10$, $k_x = 0$, $k_y = 7$. *Bottom row*: $\sigma = 5$, $k_x = 8$, $k_y = 0$; $\sigma = 5$, $k_x = 0$, $k_y = 8$; $\sigma = 10$, $k_x = 8$, $k_y = 0$; $\sigma = 10$, $k_x = 0$, $k_y = 8$

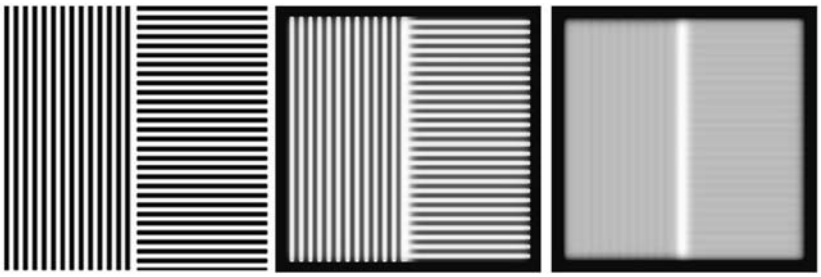

Fig. 3 Result of applying the anisotropic texture-based diffusion in (5) to an image with two well defined textures (*left*) using $\sigma = 5$, $k = 0.5$ (*center*) and $\sigma = 5$, $k = 1$ (*right*)

where $\|\nabla \mathbf{R}\|^2 = \text{trace}((\nabla \mathbf{R})^t \nabla \mathbf{R})$ (if A is a matrix, A^t denotes the transpose matrix of A). Note that diffusion is inhibited at large values of $\|\nabla \mathbf{R}\|$, i.e., at points where there is a rapid transition of the texture characteristics of the image.

We apply an explicit discretization method to discretize (5). For that we replace the gradients and divergence in (5) by discrete approximations; for any scalar function f defined on the grid $\{1, \ldots, N\} \times \{1, \ldots, M\}$ where the images are defined we shall use the notation

$$\nabla^{+,+} f = (\nabla_x^+ f, \nabla_y^+ f), \qquad \nabla^{+,-} f = (\nabla_x^+ f, \nabla_y^- f),$$
$$\nabla^{-,+} f = (\nabla_x^- f, \nabla_y^+ f), \qquad \nabla^{-,-} f = (\nabla_x^- f, \nabla_y^- f),$$

where

$$\nabla_x^+ f(i,j) = f(i+1,j) - f(i,j),$$
$$\nabla_x^- f(i,j) = f(i,j) - f(i-1,j),$$
$$\nabla_y^+ f(i,j) = f(i,j+1) - f(i,j),$$
$$\nabla_y^- f(i,j) = f(i,j) - f(i,j-1),$$

for any $(i, j) \in \{1, \ldots, N\} \times \{1, \ldots, M\}$. Note that the dual operators to $\nabla^{+,+}$, $\nabla^{+,-}$, $\nabla^{-,+}$, $\nabla^{-,-}$ are, respectively, the operators $\text{div}^{-,-}$, $\text{div}^{-,+}$, $\text{div}^{+,-}$, $\text{div}^{+,+}$ where for a discrete vector field (A, B) we have $\text{div}^{-,-}(A, B) = \nabla_x^- A + \nabla_y^- B$ and similarly for the other operators. Using $\Delta x = \Delta y = 1$, the discretization of (5) :

$$I^{t+\Delta t}(i,j) = I^t(i,j) + \frac{\Delta t}{4} \sum_{\alpha,\beta \in \{+,-\}} \text{div}^{\alpha*,\beta*}(c(\|\nabla^{\alpha,\beta}\mathbf{R}\|)\nabla^{\alpha,\beta} I)(i,j) \quad (6)$$

for any $(i, j) \in \{1, \ldots, N\} \times \{1, \ldots, M\}$, where

$$\|\nabla^{\alpha,\beta}\mathbf{R}(i,j)\| = \sqrt{\sum_{1 \le s \le S} \sum_{-N \le n_x \le N} \sum_{0 \le n_y \le N} |\nabla^{\alpha,\beta} F^s_{n_x,n_y}(i,j)|^2}.$$

We apply a wide range of filters varying the scale and frequency. In order to reduce the computational cost, we have only used horizontally and vertically oriented Gabor filters and thus, the discretization of gradient magnitude has also been performed in these two orientations. Although this is not rotationally invariant, the filtered image will be used to obtain the initial pre-segmentation, which will be improved later using the active contours.

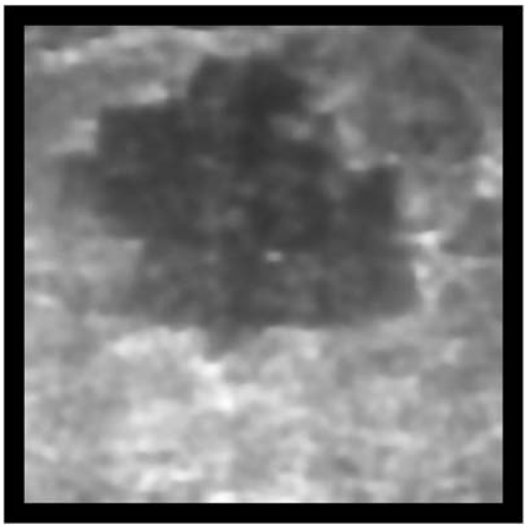

Fig. 4 Result of applying the anisotropic texture-based diffusion in (5) to the nodule in Fig. 1, using $S = 3$ ($\sigma_0 = 3$) and $N = 4$ ($k_0 = 0.05$)

Figure 3 shows the application of this kind of filtering to well defined textures, and how the variation of the frequencies modifies the results. For that reason, it is necessary to use a wide enough range of values. Figure 4 shows the result of this kind of anisotropic texture-based diffusion of ultrasound images. As observed, not only does it reduce speckle noise, but it also preserves the significant edges, so that a semiautomatic pre-segmentation of the nodule is more feasible and trustful.

3 Front Propagation Pre-segmentation

The result of the filter described in the previous section is much more suitable for a pre-segmentation than the original image. A simple approach consists in applying a region-growing algorithm, which, from an initial inner point, expands the selected region while the magnitude of the gradient is lower than a certain threshold. However, ultrasound images do not always present uniform and well-defined

edges, which makes it extremely difficult to set a threshold for the gradient magnitude. This causes the selection to be either limited to the central region of the nodule, or overflowed towards the outer regions. We propose the use of a gradient-guided front propagation scheme.

To obtain a robust computation of the modulus of the gradient of the image I (where I denotes the output of the diffusion equation (5)), we compute the structure tensor

$$G_\sigma * (\nabla I \otimes \nabla I) := \begin{pmatrix} G_\sigma * I_x^2 & G_\sigma * (I_x I_y) \\ G_\sigma * (I_x I_y) & G_\sigma * I_y^2 \end{pmatrix}, \quad (7)$$

where G_σ is a Gaussian kernel and I_x and I_y are calculated using the following 3×3 masks:

$$\frac{1}{4h}\begin{pmatrix} -b & 0 & b \\ -a & 0 & a \\ -b & 0 & b \end{pmatrix} \quad \text{and} \quad \frac{1}{4h}\begin{pmatrix} -b & -a & -b \\ 0 & 0 & 0 \\ b & a & b \end{pmatrix}, \quad (8)$$

where $a = 2(\sqrt{2}-1)$ and $b = (2-\sqrt{2})$. The largest eigenvalue gives us an estimate of the square of the modulus gradient and we shall use it as a robust estimation of it. We denote it by $\lambda^+(G_\sigma * (\nabla I \otimes \nabla I))$ (for more details about the structure tensor, see [3]).

To obtain a good snake initialization, we use a balloon force in a level set formulation. Starting with an initial parameterized curve $C_0 : [0, L] \to \mathbb{R}^2$, $L > 0$, in the image domain we use a front which propagates outwards with a speed depending inversely on the modulus of the gradient:

$$\frac{\partial C}{\partial t} = F\mathbf{n}, \quad (9)$$

where $C(t) : [0, L] \to \mathbb{R}^2$ denotes the evolving curve, $t > 0$ denotes time parameter of the evolution, and

$$F(x, y) = \frac{1}{1 + G_\eta * \lambda^+(G_\sigma * (\nabla I \otimes \nabla I))(x, y)}, \quad (10)$$

G_η being a Gaussian of standard deviation η. To fix ideas, we assume that $C(t)$ is clockwise oriented and $\mathbf{n}$ denotes the outer unit normal to C. We want the propagation to stop when the contour of the nodule is reached. For that reason, the function F is inhibiting the propagation proportionally to the magnitude of the gradient in the neighborhood of each pixel, in such a way that when we are far from the contour, the front propagates faster, but, as we approach the contour, the speed is reduced. Following Appendix 1 we introduce a evolving function $u(t, x, y)$ whose zero level set is the curve $C(t)$ (positive inside and negative outside $C(t)$) and we write the geometric evolution for C in terms of u as

$$\frac{\partial u}{\partial t} = F\|\nabla u\|. \quad (11)$$

To discretize it, we have used the following numerical scheme:

$$\frac{u_{i,j}^{n+1} - u_{i,j}^n}{\tau} = F_{i,j}\|\nabla u_{ij}\|, \quad (12)$$

where $F_{i,j}$ is the discretization of $F(x, y)$ given by (10) (using the approximations of the gradient of I described in (8) and a suitable discretization of the Gaussian window) and $\|\nabla u_{ij}\|$ is calculated as in [29]:

$$\begin{aligned} \|\nabla u_{ij}\| = &\left(\min\left(\frac{u_{i,j}^n - u_{i-1,j}^n}{h_1}, 0\right)\right)^2 \\ &+ \left(\max\left(\frac{u_{i+1,j}^n - u_{i,j}^n}{h_1}, 0\right)\right)^2 \\ &+ \left(\min\left(\frac{u_{i,j}^n - u_{i,j-1}^n}{h_2}, 0\right)\right)^2 \\ &+ \left(\max\left(\frac{u_{i,j+1}^n - u_{i,j}^n}{h_2}, 0\right)\right)^2. \end{aligned} \quad (13)$$

In these equations, τ represents the time discretization step and h_1, h_2 the pixel dimensions ($\tau, h_1, h_2 > 0$; in our experiments, we consider $h_1, h_2 = 1$). Figure 5 displays the evolution of the front when I is given in Fig. 4. Figure 6 displays the pre-segmentation which is obtained. Once a whole contour with high enough gradients is reached or the maximum number of iterations have been performed, the process is stopped and the final front is used as initial approximation $P_i(\tilde{s})$ for the active contours technique.

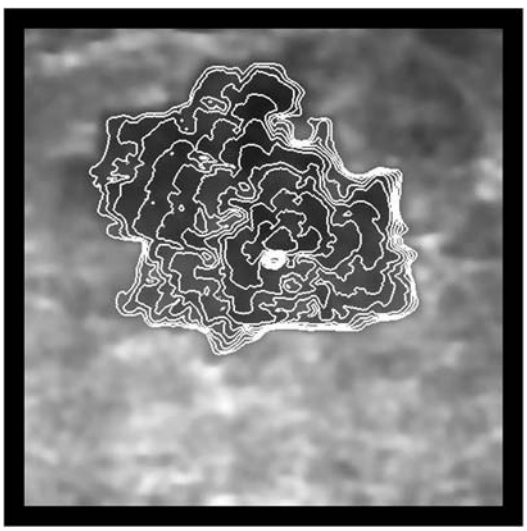

Fig. 5 Evolution of the front propagation using the gradient-weighted propagation scheme

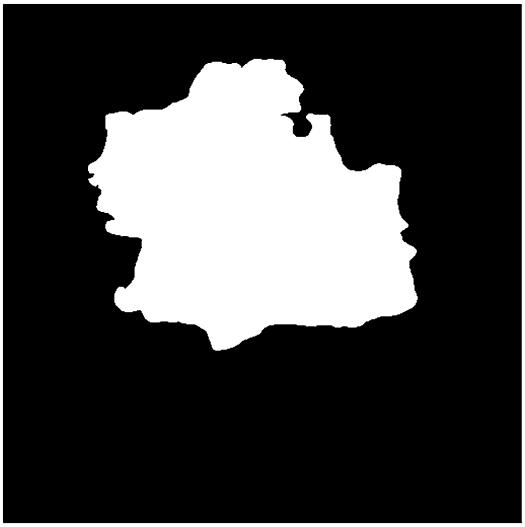

Fig. 6 Presegmentation obtained using the front propagation scheme with gradient weighting. A threshold is set on the graylevel to determine the points which are included in the presegmentation

4 Vector-Based Geodesic Active Contours

The front propagation scheme does not provide satisfactory results, since its speed of propagation is a function of magnitude of the gradient and we cannot find a single threshold on it to determine the desired contour. The segmentation which can be obtained through this kind of algorithms in the case of ultrasound images is often inaccurate. A more refined contour can be extracted using geodesic active contours [5, 6, 23].

4.1 Classical Geodesic Active Contours

Geodesic active contours are based on the minimization of the following energy:

$$E_{\text{gac}}(C) = \int_C g_\sigma(C(s))\, ds, \tag{14}$$

where $C : [0, L] \to \mathbb{R}^2$, $L > 0$, is a rectifiable curve parameterized by arc-length s and ds denotes the arc-length element. The function $g_\sigma(x, y)$ is a smooth decreasing function of the modulus of the gradient of a regularized version of the image $I(x, y)$ on which the segmentation is performed, and C is the snake with respect to which the energy is minimized. To minimize the energy (14) we use a gradient descent curve evolution written as

$$C_t = -\frac{\delta E_{\text{gac}}(C)}{\delta C}, \tag{15}$$

where $\frac{\delta E_{\text{gac}}(C)}{\delta C}$ represents the first variation of E_{gac}. Computing the first variation of E we obtain (see [6, 7]) the curve evolution equation

$$C_t = -(\kappa g_\sigma - \langle \nabla g_\sigma, \mathbf{n} \rangle)\mathbf{n}, \tag{16}$$

where κ denotes the curvature of C. The function $g_\sigma(x, y)$ acts as an edge detector and, as in [4, 6], we shall use

$$g_\sigma(I) = \frac{1}{\sqrt{1 + \alpha \|\nabla I_\sigma\|^2}}, \tag{17}$$

where I_σ represents the convolution of the original image I with a Gaussian kernel with standard deviation σ. The parameter α controls how contrasted the edges must be to stop the evolution. On the other hand, σ determines the amount of smoothing of I, so that a higher value will produce a more rounded contour but will be able to reach farther edges. For this reason, we use a multiscale implementation, starting with higher values of σ and reducing it at each scale. We use the final contour of the previous scale as initialization, except for the first case, in which the initialization is provided by the pre-segmentation step. Thus, given a final standard deviation σ_0 and a number of scales $\widehat{S}$, the standard deviations used at the different scales are $\widehat{S}\sigma_0$, $(\widehat{S} - 1)\sigma_0, \ldots, \sigma_0$.

To write the level set formulation of (16) as described in Appendix 1, we introduce a function $u(t, x, y)$ as an implicit representation of $C(t)$. Usually, to construct the initial snake $u(0, x, y)$, the user has to choose a set of points determining a parameterization of a polygon $P_0(\tilde{s}) = (x_0(\tilde{s}), y_0(\tilde{s}))$ and then define $u(0, x, y)$ so that $P_0(\tilde{s})$ corresponds to the zero level set of $u(0, x, y)$. In our case, instead of manually defining $P_0(\tilde{s})$, we take the curve $P_i(\tilde{s})$ computed with the propagation scheme discussed in Sect. 3 and given by the PDE (9). Then, we define $u(0, x, y)$ as the signed distance function to $P_i(\tilde{s})$ (positive inside, negative outside), or simply consider two different values for the inner and outer regions.

As described in Appendix 1, the level set formulation of the geometric curve evolution (16) is given by the PDE:

$$\frac{\partial u}{\partial t} = \|\nabla u\| \text{div}\left(g_\sigma(I) \frac{\nabla u}{\|\nabla u\|} \right). \tag{18}$$

If we expand this equation, we obtain the following expression, in which the first term controls the smoothness of the contour and the second one makes the contour evolve towards the highest gradients:

$$\frac{\partial u}{\partial t} = \|\nabla u\| g_\sigma(I) \text{div}\left(\frac{\nabla u}{\|\nabla u\|} \right) + \nabla u \nabla g_\sigma(I). \tag{19}$$

It may be desirable in some cases to re-balance the contribution of both terms. For that purpose, we introduce a parameter $\lambda > 0$ which helps us adjust the results to the desired conditions:

$$\frac{\partial u}{\partial t} = g_\sigma(I) \|\nabla u\| \text{div}\left(\frac{\nabla u}{\|\nabla u\|} \right) + \lambda \nabla u \nabla g_\sigma(I). \tag{20}$$

Geodesic active contours permit to improve the presegmentation obtained using (11) since the contour adapts

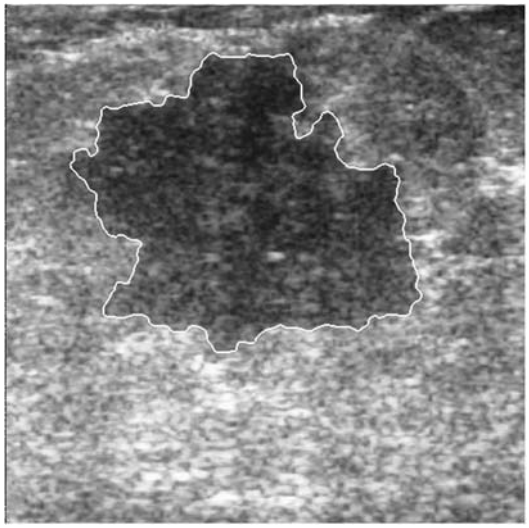

Fig. 7 Final contour obtained for the nodule in Fig. 1 using the geodesic active contours scheme in (14) from the front propagation presegmentation

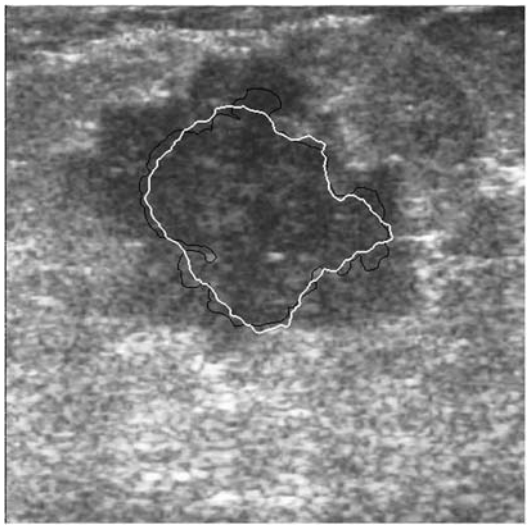

Fig. 8 Final contour (white) obtained for the nodule in Fig. 1 using the geodesic active contours scheme in (14) from the initial curve depicted in black. This shows the usefulness of a reasonable initial presegmentation

to the minimum of the energy (14). In Fig. 7 we display the resulting contour obtained using the multiscale implementation of the geodesic active contours (20) with the value of $\lambda = 5$. The details of the numerical implementation can be found in Appendix 2.

As mentioned above, it is important to start from a presegmentation which is relatively close to the real contour of the nodule. Otherwise, the effect of the second term in (20) (or (19)) is not enough to overcome the regularizing effect of the first term and instead of approaching the real edges, the snake will be rounded and tend to reduce, as illustrated in Fig. 8.

4.2 Region Information in Geodesic Active Contours Using a Single Feature Descriptor

In the classical active contours technique, only intensity gradient is considered as a descriptor for the limits of the regions, in such a way that the terms in equation (14) guide the snake towards those points where a high gradient is present. However, sometimes a region is not clearly identified by high gradient edges, or these are not uniformly high along the outline of an object, thus making it difficult to set the parameters. The intensity of the surrounding area and the texture described by the gray level pattern play an important role in delimiting the inner and outer regions. This often happens in ultrasound images, and new terms must be added to provide this technique with the capability of identifying these low contrast boundaries. If we have a gradual transition from a region to the other, no high gradient contour will be found to identify the limits. Geodesic active regions include region information in the evolution of the snake, so that the features that describe the inner and outer regions make the contour evolve [9, 30].

If we consider a single feature to separate two regions, such as gray level, we can use the distance to the representative values of the inner and outer regions to make the contour evolve. The purpose consists in finding the curve whose inner and outer regions are jointly best represented by these values. If the inner and outer regions are quite homogeneous and the contour is uniform, we can use the global representatives of both regions for all the points. If C denotes the evolving contour, the above considerations lead to the minimization of the energy functional

$$E_s(C, \tilde{c}_+, \tilde{c}_-) = E_{\text{gac}}(C) + E_m(C, \tilde{c}_+, \tilde{c}_-), \tag{21}$$

where

$$E_m(C, \tilde{c}_+, \tilde{c}_-) = \lambda_+ \int_{\Omega_C} |I(x, y) - \tilde{c}_+| \, dxdy + \lambda_- \int_{\Omega \setminus \Omega_C} |I(x, y) - \tilde{c}_-| \, dxdy, \tag{22}$$

where Ω_C denotes the region inside C (that is the complement of the unbounded component of $\mathbb{R}^2 \setminus C$) and $\lambda_+, \lambda_- > 0$ are fixed parameters. The first term is the usual geodesic active contour term, the second and third terms are like the so-called piecewise-constant two-phase Mumford–Shah model and are region based [9, 30]. We notice that the energy $E_s(C, \tilde{c}_+, \tilde{c}_-)$ is minimized with respect to the curve C and the constants $\tilde{c}_+, \tilde{c}_-$ which describe the image I inside and outside C, respectively.

To compute the first variation of (22) we recall the following result [7, 24].

Lemma 1 *Let $f:\mathbb{R}^2\to\mathbb{R}$ be an integrable function. The weighted region functional*

$$E_f(C)=\iint_{\Omega_C} f(x,y)dxdy,$$

yields the first variation

$$\frac{\delta E_f(C)}{\delta C}=-f(x,y)\vec{n}.$$

Using the first variation of the energy (14) and Lemma 1 we compute the first variations of $E_s(C,\tilde{c}_+,\tilde{c}_-)$:

$$\frac{\delta E_s}{\delta C}=(\kappa g_\sigma-\langle\nabla g_\sigma,\mathbf{n}\rangle)\mathbf{n}+M(I,\tilde{c}_+,\tilde{c}_-)(x,y)\mathbf{n},$$

where

$$M(I,\tilde{c}_+,\tilde{c}_-)(x,y)=\lambda_-|I(x,y)-\tilde{c}_-|-\lambda_+|I(x,y)-\tilde{c}_+|, \tag{23}$$

$$\frac{\delta E_s}{\delta\tilde{c}_+}=\lambda_+\int_{\Omega_C}\operatorname{sign}(\tilde{c}_+-I(x,y))\,dxdy,$$

$$\frac{\delta E_s}{\delta\tilde{c}_-}=\lambda_-\int_{\Omega\setminus\Omega_C}\operatorname{sign}(\tilde{c}_--I(x,y))\,dxdy,$$

where $\operatorname{sign}(r)=+1$ if $r>0$; -1 if $r<0$; and it can be any value in $[-1,1]$ if $r=0$.

For fixed C the minimum values of $\tilde{c}_+$ and $\tilde{c}_-$ satisfy

$$\frac{\delta E_s}{\delta\tilde{c}_+}=0\quad\text{and}\quad\frac{\delta E_s}{\delta\tilde{c}_-}=0.$$

These equations give the values of $\tilde{c}_+$, $\tilde{c}_-$ explicitly. Heuristically, the optimal value of $\tilde{c}_+$, resp. $\tilde{c}_-$, is the value of $I(x,y)$ in Ω_C, resp. $\Omega\setminus\Omega_C$, that splits its area into two equal parts. These values are the median values

$$\tilde{c}_+=\operatorname{median}_{\Omega_C}(I),\qquad\tilde{c}_-=\operatorname{median}_{\Omega\setminus\Omega_C}(I). \tag{24}$$

The gradient descent equation for the evolving curve C is

$$C_t=-\frac{\delta E_s}{\delta C}=-(\kappa g_\sigma-\langle\nabla g_\sigma,\mathbf{n}\rangle)\mathbf{n}-M(I,C(t))(x,y)\mathbf{n}, \tag{25}$$

where

$$M(I,C(t))(x,y)=M(I,\tilde{c}_+(t),\tilde{c}_-(t))(x,y),$$

where $\tilde{c}_+(t),\tilde{c}_-(t)$ are the median values given in (24) for the curve $C(t)$.

However, in the case of ultrasound images we deal with very variable contours and heterogeneous regions. This is the reason why we have used, for every point, the medians of the inner and outer neighborhoods, so that the evolution of the curve depends on the region where we are located. We propose to localize the energy (22). For that, for any rectifiable curve C and functions $c_+(x,y)$, $c_-(x,y)$, we define the energy functional

$$E_{sl}(C,c_+,c_-)=E_{\text{gac}}(C)+E_{ml}(C,c_+,c_-), \tag{26}$$

where

$$\begin{aligned}E_{ml}(C,c_+,c_-)&=\lambda_+\int_\Omega\left(\int_{\Omega_C\cap B(x,y)}|I(x',y')-c_+(x,y)|\,dx'dy'\right)dxdy\\&\quad+\lambda_-\int_\Omega\left(\int_{B(x,y)\setminus\Omega_C}|I(x',y')\right.\\&\quad\left.-c_-(x,y)|\,dx'dy'\right)dxdy,\end{aligned} \tag{27}$$

where $B(x,y)$ is a ball around (x,y) of fixed radius, and $\lambda_+,\lambda_->0$ are fixed parameters.

We denote by $\chi_A(x,y)$ the characteristic function of a set $A\subset\mathbb{R}^2$, i.e., $\chi_A(x,y)=1$ if $(x,y)\in A$ and 0 otherwise. To compute the first variations of $E_s(C,c_+,c_-)$ we observe that $\chi_{B(x',y')}(x,y)=\chi_{B(x,y)}(x',y')$ and using this we have

$$\begin{aligned}&\int_\Omega\left(\int_{\Omega_C\cap B(x,y)}|I(x',y')-c_+(x,y)|\,dx'dy'\right)dxdy\\&=\int_{\Omega_C}\left(\int_\Omega\chi_{B(x',y')}(x,y)|I(x',y')\right.\\&\quad\left.-c_+(x,y)|\,dxdy\right)dx'dy'\\&=\int_{\Omega_C}\left(\int_{\Omega\cap B(x',y')}|I(x',y')-c_+(x,y)|\,dxdy\right)dx'dy'.\end{aligned}$$

Using this, the first variation of the energy (14) and Lemma 1 we compute the first variations of $E_s(C,c_+,c_-)$:

$$\frac{\delta E_{sl}}{\delta C}=(\kappa g_\sigma-\langle\nabla g_\sigma,\mathbf{n}\rangle)\mathbf{n}+M_l(I,c_+,c_-)(x,y)\mathbf{n},$$

where (changing (x,y) and (x',y'))

$$\begin{aligned}&M_l(I,c_+,c_-)(x,y)\\&=\lambda_-\int_{\Omega\cap B(x,y)}|I(x,y)-c_-(x',y')|\,dx'dy'\\&\quad-\lambda_+\int_{\Omega\cap B(x,y)}|I(x,y)-c_+(x',y')|\,dx'dy',\end{aligned}$$

$$\frac{\delta E_{sl}}{\delta c_+} = \lambda_+ \int_{\Omega_C \cap B(x,y)} \text{sign}(c_+(x,y) - I(x',y'))\, dx'dy',$$
$$\frac{\delta E_{sl}}{\delta c_-} = \lambda_- \int_{B(x,y)\setminus\Omega_C} \text{sign}(c_-(x,y) - I(x',y'))\, dx'dy'.$$

For fixed C the minimum values of $c_+(x,y)$ and $c_-(x,y)$ satisfy $\frac{\delta E_s}{\delta c_+} = 0$ and $\frac{\delta E_s}{\delta c_-} = 0$. Heuristically, the optimal value of $c_+(x,y)$, resp. $c_-(x,y)$, is the value of $I(x,y)$ in $\Omega_C \cap B(x,y)$, resp. $B(x,y)\setminus\Omega_C$, that splits its area into two equal parts. These values are the median values

$$\begin{aligned} c_+(x,y) &= \text{median}_{\Omega_C \cap B(x,y)}(I), \\ c_-(x,y) &= \text{median}_{B(x,y)\setminus\Omega_C}(I). \end{aligned} \tag{28}$$

The gradient descent equation for the evolving curve C is

$$\begin{aligned} C_t &= -\frac{\delta E_{sl}}{\delta C} \\ &= -(\kappa g_\sigma - \langle \nabla g_\sigma, \mathbf{n}\rangle)\mathbf{n} - M_l(I, C(t))(x,y)\mathbf{n}, \end{aligned} \tag{29}$$

where

$$M_l(I, C(t))(x,y) = M_l(I, c_+(t), c_-(t))(x,y),$$

where $c_+(t,x,y), c_-(t,x,y)$ are the median values given in (28) for the curve $C(t)$.

As described in Appendix 1 the level set formulation of the gradient descent equation corresponding to (27) is

$$\begin{aligned} \frac{\partial u}{\partial t} &= \|\nabla u\| \text{div}\left(g_\sigma(I) \frac{\nabla u}{\|\nabla u\|} \right) \\ &\quad + \|\nabla u\| M_l(I, [u(t) \geq 0]). \end{aligned} \tag{30}$$

For computational simplicity, assuming that $c_+(x',y')$ and $c_-(x',y')$ are approximately constant in $B(x,y)$, we may approximate $M_l(C, c_+, c_-)$ by

$$\begin{aligned} M_{l,\text{app}}(, c_+, c_-) &= \lambda_- V |I(x,y) - c_-(x,y)| \\ &\quad - \lambda_+ V |I(x,y) - c_+(x,y)|, \end{aligned}$$

where V is the area (number of pixels) of the ball $B(x,y)$. Since V is a constant value, it can be reabsorbed in the parameters λ_+, λ_-. In our experiments, we shall use $\lambda_+ = \lambda_- = \beta$. In this case, we use the level set formulation

$$\begin{aligned} \frac{\partial u}{\partial t} &= \|\nabla u\| \text{div}\left(g_\sigma(I) \frac{\nabla u}{\|\nabla u\|} \right) \\ &\quad + \|\nabla u\| M_{l,\text{app}}(I, [u(t) \geq 0]). \end{aligned} \tag{31}$$

Developing the divergence term we may weight the term $\nabla g_\sigma(I) \cdot \nabla u$ with a factor λ as in (20).

An alternative approach could be to use the (local) mean and the variance of the regions in a similar way as we have done using the median, by replacing the term M_l by a combination of the following ones

$$\begin{aligned} &M_m(I, m_+, m_-)(x,y) \\ &= \lambda_{m-} \int_{\Omega \cap B(x,y)} |I(x,y) - m_-(x',y')|^2\, dx'dy' \\ &\quad - \lambda_{m+} \int_{\Omega \cap B(x,y)} |I(x,y) - m_+(x',y')|^2\, dx'dy', \end{aligned} \tag{32}$$

$$\begin{aligned} &M_v(I, m_+, m_-, v_+, v_-)(x,y) \\ &= \lambda_{v-} \int_{\Omega \cap B(x,y)} |(I(x,y) - m_-(x',y'))^2 \\ &\quad - v_-(x',y')|\, dx'dy' \\ &\quad - \lambda_{v+} \int_{\Omega \cap B(x,y)} |(I(x,y) - m_+(x',y'))^2 \\ &\quad - v_+(x',y')|\, dx'dy', \end{aligned} \tag{33}$$

where $m_-(x,y)$ is mean of I in $B(x,y)\setminus\Omega_C$, $m_+(x,y)$ is the mean of I in $\Omega_C \cap B(x,y)$, and $v_-(x,y)$ and $v_+(x,y)$ are the corresponding variances in $B(x,y)\setminus\Omega_C$ and $\Omega_C \cap B(x,y)$, respectively.

The median is quite robust to the possible extreme values, such as those observed when the nodule presents calcifications. Furthermore, the use of local values allows identifying parts of the contour which present different degrees of contrast, since the use of global descriptors makes it very difficult to extract values which allow identifying the whole contour.

4.2.1 A Variant of Model (31)

We can observe that the last term in (31) is locally isotropic, since it only depends on the magnitude of ∇u, and not on its orientation. In order that the behavior of the median in a neighborhood of the point helps moving the level set in the right direction in a more explicit way, we have introduced a second alternative, again to be used when our initial contour is not far from the desired one. We can use the gradient of the distance to guide the evolution of the snake in order to find those points which are as far from the medians of such feature in the inner and outer regions. Since we can be outside or inside the right border, the absolute value is taken. This alternative considers the variation of the difference with respect to the medians in the neighborhood of the points and, consequently, allows tackling the problems of isolated outlying points and high local variations. If we consider intensity, this results in the following equation:

$$\frac{\partial u}{\partial t} = \|\nabla u\| \text{div}\left(g_\sigma(I) \frac{\nabla u}{\|\nabla u\|} \right) + \nabla u \cdot \nabla \widehat{M}(I,u), \tag{34}$$

where

$$\begin{aligned} \widehat{M}(I,u)(x,y) &= |\lambda_- |I(x,y) - c_-(x,y)| \\ &\quad - \lambda_+ |I(x,y) - c_+(x,y)||. \end{aligned} \tag{35}$$

Fig. 9 Example of the use of region information. *Left*: nodule with diffuse contours. *Center*: the inner contour is an example of a bad initialization of the snake. We have computed the values of M for this initialization and we have depicted in dark gray the values which are negative and in light gray the values which are positive. The outer contour is the validated one provided by the physicians. As observed, the function M changes its sign very close to the validated contour. *Right*: we have computed $\widehat{M}$ using the same bad initialization. As observed, the function has a minimum close to the validated contour provided by the physicians

When $\widehat{M}(x, y) = 0$, the value $I(x, y)$ is equidistant to the medians of I at the points in the neighborhood of (x, y) which are outside and inside the snake. On the other hand, the higher the value of the modulus of $\nabla\widehat{M}$, the farther the border, and the term $\nabla u \cdot \nabla\widehat{M}$ will make the contour evolve towards the border. Figure 9 shows an example with a nodule with diffuse contours for which M and $\widehat{M}$ have been calculated for a given initialization of the snake which is far from the validated segmentation provided by the specialists. As observed, M changes its sign when approaching the validated contour, while $\widehat{M}$ has a minimum in that region. Both, the minimum of $\widehat{M}$ and the sign change of M are much closer to the right contour (external one) than the initial approximation for which they have been calculated (internal one).

4.3 Region Information in Geodesic Active Contours Using a Vectorial Descriptor

Not only intensity determines the limits of regions. The texture described by the gray level pattern plays an important role in delimiting the inner and outer regions, specially if we work with ultrasound images. As in [8], our approach considers the responses of a set of Gabor filters in its vectorial form, and tries to use this information to obtain a texture-guided segmentation. As in Sect. 4.2, we have tested two different ways of including this region information into the active contour equation. The first one corresponds to the local version of the model introduced in [8] (see also [10, 34]) (we use a robust term), and aims at attracting the snakes towards the edges of the texture description: as in the case of a single feature, we consider, for every point, the median values of the inner and outer neighborhoods. For that, for any rectifiable curve C and functions $\vec{c}_+(x, y) = (c_+^1(x, y), \ldots, c_+^m(x, y))$, $\vec{c}_-(x, y) = (c_-^1(x, y), \ldots, c_-^m(x, y))$, we define the energy functional

$$E_G(C, \vec{c}_+, \vec{c}_-) = E_{\text{gac}}(C) + E_{Gml}(C, \vec{c}_+, \vec{c}_-) \tag{36}$$

where

$$\begin{aligned} &E_{Gml}(C, \vec{c}_+, \vec{c}_-) \\ &= \sum_{1\le i\le m} \lambda_+^i \int_\Omega \Bigg(\int_{\Omega_C \cap B(x,y)} |I^i(x', y') \\ &\quad - c_+^i(x, y)|\, dx'dy' \Bigg) dxdy \\ &\quad + \sum_{1\le i\le m} \lambda_-^i \int_\Omega \Bigg(\int_{B(x,y)\setminus\Omega_C} |I^i(x', y') \\ &\quad - c_-^i(x, y)|\, dx'dy' \Bigg) dxdy, \end{aligned} \tag{37}$$

where I^i, $i = 1, \ldots, m$, are the responses to m Gabor filters of the original image, obtained for different scales, orientations, and frequencies, and $\lambda_+^i, \lambda_-^i > 0$ are fixed parameters for each channel. As explained before, the first term is the usual geodesic active contour term, but here the second and third terms are region based active contours based on Gabor feature space for the segmentation of textured images [8, 34]. The energy is minimized with respect to C, $\vec{c}_+$ and $\vec{c}_-$. At the minimum, $c_+^i(x, y)$, $c_-^i(x, y)$ are the median values of the Gabor channel I^i around (x, y) inside and outside the curve C, respectively.

As in Sect. 4.2, equating to zero the first variations of $E_G(C, \vec{c}_+, \vec{c}_-)$ with respect to c_+^i and c_-^i, $i = 1, \ldots, m$, we obtain

$$c_+^i(x, y) = \text{median}_{\Omega_C \cap B(x,y)}(I^i),$$
$$c_-^i(x, y) = \text{median}_{B(x,y)\setminus\Omega_C}(I^i).$$

Now, computing the first variation of $E_G(C, \vec{c}_+, \vec{c}_-)$ with respect to C and writing the gradient descent equation for C

$$C_t = -\frac{\delta E}{\delta C}$$

in a level set formulation (see Appendix 1) we obtain the PDE:

$$\frac{\partial u}{\partial t} = \|\nabla u\| \operatorname{div}\left(g_\sigma(I) \frac{\nabla u}{\|\nabla u\|} \right) + \|\nabla u\| M_G(I,u), \tag{38}$$

where

$$\begin{aligned} &M_G(I,u)(x,y) \\ &= \sum_{1\le i\le m} \lambda_-^i \int_{\Omega\cap B(x,y)} |I^i(x,y) - c_-^i(x',y')|\,dx'dy' \\ &\quad - \sum_{1\le i\le m} \lambda_+^i \int_{\Omega\cap B(x,y)} |I^i(x,y) - c_+^i(x',y')|\,dx'dy'. \end{aligned}$$

As in Sect. 4.2, if we assume that the functions $c_+^i(x,y)$, $c_-^i(x,y)$, $i=1,\dots,m$, are approximately constant in $B(x,y)$ we may approximate $M_G(I,u)(x,y)$ by

$$\begin{aligned} &M_{G,\mathrm{app}}(I,u)(x,y) \\ &= \sum_{1\le i\le m} \lambda_-^i |I^i(x,y) - c_-^i(x,y)| \\ &\quad - \sum_{1\le i\le m} \lambda_+^i |I^i(x,y) - c_+^i(x,y)|, \end{aligned} \tag{39}$$

where we have normalized the area of $B(x,y)$ to 1 (which amounts to reabsorb this area in the notation of λ_+^i, λ_-^i) and consider the PDE (38) with $M_G(I,u)$ replaced by $M_{G,\mathrm{app}}(I,u)$. As done with the single feature scheme, we have also taken $\lambda_+^i = \lambda_-^i = \beta > 0$ for any $i=1,\dots,m$.

When $M_{G,\mathrm{app}}(I,u)(x,y) = 0$, the outputs of the Gabor filters at (x,y) are equidistant from the medians of the outputs of the respective filters in the outer and inner regions of C around (x,y). When $M_{G,\mathrm{app}} < 0$, the outputs at that point are closer to those outside than to those inside, so that its value must be decreased. When $M_{G,\mathrm{app}} > 0$, the opposite occurs and its value must be increased.

4.3.1 A Variant of Model (38)

Recall that our purpose is to identify the contour separating two regions whose local median responses are different and separated by a smooth transition of the texture descriptors. Arguing as in Sect. 4.2.1, if the changes in the texture are reflected as changes in the filter responses and, if they are gradual, the contour can be identified as the set of points where the response is equidistant to the response on both regions. This leads to the following equation:

$$\frac{\partial u}{\partial t} = \|\nabla u\| \operatorname{div}\left(g_\sigma(I) \frac{\nabla u}{\|\nabla u\|} \right) + \nabla u \cdot \nabla \widehat{M}_G(I,u_0), \tag{40}$$

where $\widehat{M}_G$ is given by

$$\widehat{M}_G(I,u)_{x,y} = |M_G(I,u)(x,y)|. \tag{41}$$

As in the previous case, when $\widehat{M}_G(I,u)_{x,y} = 0$, the outputs of the Gabor filters at (x,y) are equidistant to the medians of the outputs of the respective filters in the outer and inner neighborhoods of (x,y). However, in this case, $\widehat{M}_G$ increases as we leave the edges (its gradient points out of the edges). Consequently, the term $\nabla u \cdot \nabla \widehat{M}_G(I,u_0)$ moves the snake towards the edges.

5 Results

The accuracy of the different models which have been proposed has been tested using the manual segmentations carried out by the specialists. The mean distance from the points in the semi-automatic segmentation to those in the manual one and vice versa is a suitable measure of the precision obtained.

Table 1 shows both distances and their mean for the presegmentation schemes proposed above (we have used the values $\alpha = 0.1$, $\lambda = 5$, $\sigma = 2$, $\beta = 0.1$, 3 scales and 1000 iterations per scale). The selection of the values for the different parameters depends on the importance that the edge contrast, the roundness of the contour or the texture pattern are given. The results of the anisotropic texture-based diffusion (AD) are compared with those of the non-filtered image (NF) and the truncated median filter (TM) [16] to show the

Table 1 Comparison of the distances to/from the validated manual segmentation for the presegmentations using different types of filters (NF = no filtering, TM = truncated median, AD = anisotropic diffusion, RG = region growing, FP = front propagation)

Presegmentation	To manual	From manual	Mean
NF + RG	13.10	10.86	11.98
NF + FP	16.37	14.30	15.34
TM + RG	10.15	10.45	10.30
TM + FP	11.72	7.35	9.53
AD + RG	10.73	10.27	10.50
AD + FP	9.96	4.90	7.43

Table 2 Comparison of the distances to/from the validated manual segmentation for the geodesic active contours and geodesic active regions (GAC = geodesic active contours, NRI = no region information, MR = medians of regions, GMR = medians of Gabor features in regions)

Segmentation	To manual	From manual	Mean
Basic GAC	4.10	4.53	4.31
NRI	3.85	4.20	4.03
MR ($M(I,u)$)	3.85	4.20	4.03
MR ($\nabla\widehat{M}(I,u)$)	3.92	4.01	3.96
GMR ($M_G(I,u)$)	3.85	4.20	4.03
GMR ($\nabla\widehat{M}_G(I,u)$)	3.85	3.57	3.71

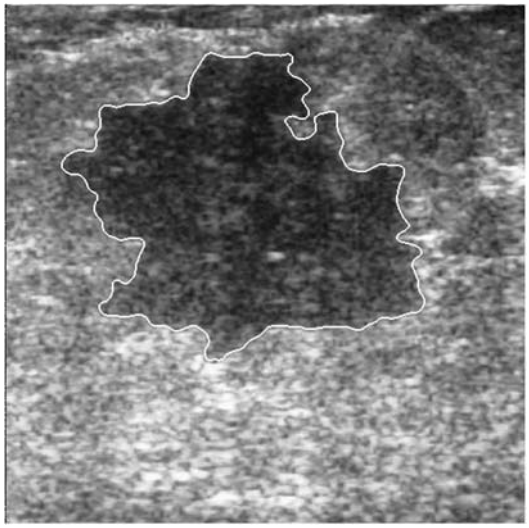

Fig. 10 Final contour obtained for the nodule in Fig. 1 using the geodesic active contours scheme in (41) with Gabor filters from the front propagation presegmentation (we have used the values $\alpha = 0.1$, $\lambda = 5$, $\sigma = 2$, $\beta = 0.1$, 3 scales and 1000 iterations)

accuracy of two types pre-segmentations: a region-growing algorithm (RG) and the front propagation scheme (FP). On the other hand, Table 2 compares the same distances once the geodesic active contours with region information are applied. The basic geodesic active contours technique (GAC) is improved by performing more iterations considering different terms. The scheme with no region information (NRI) is compared with the one described in (27) for median intensity separable regions (MR) using (30) and (34), and with that described in (38) and (40) for Gabor descriptors medians (GMR). Figure 10 illustrates the result of applying geodesic active regions with Gabor descriptors.

As mentioned above, we have used the local median as a region descriptor to improve the separation between the nodule and the surrounding tissues. However, other statistical descriptors could also be used. Figure 11 illustrates the differences between using the median or a combination of the mean and the variance as region descriptors. For that, we extended the terms $M_G(I,u)$ or $\widehat{M}_G(I,u)$ by the corresponding ones which use the local mean and variance (see (32) and (33)). The robustness of the median allows a satisfactory identification of the boundaries, even when dealing with noisy regions with disturbing values or low contrast areas. The results obtained using the local mean and variance are equally satisfactory, though the median was negligibly better. Furthermore, Fig. 11 shows that the use of local descriptors, instead of global ones, permits to adjust the evolution of the snake to the characteristics of the region, in such a way that those nodules which present a non-uniform contrast with the surrounding tissues along the contour are also properly delimited. If we use global descriptors, it is difficult to find representative values which are suitable for the whole contour, and local descriptors provide better results.

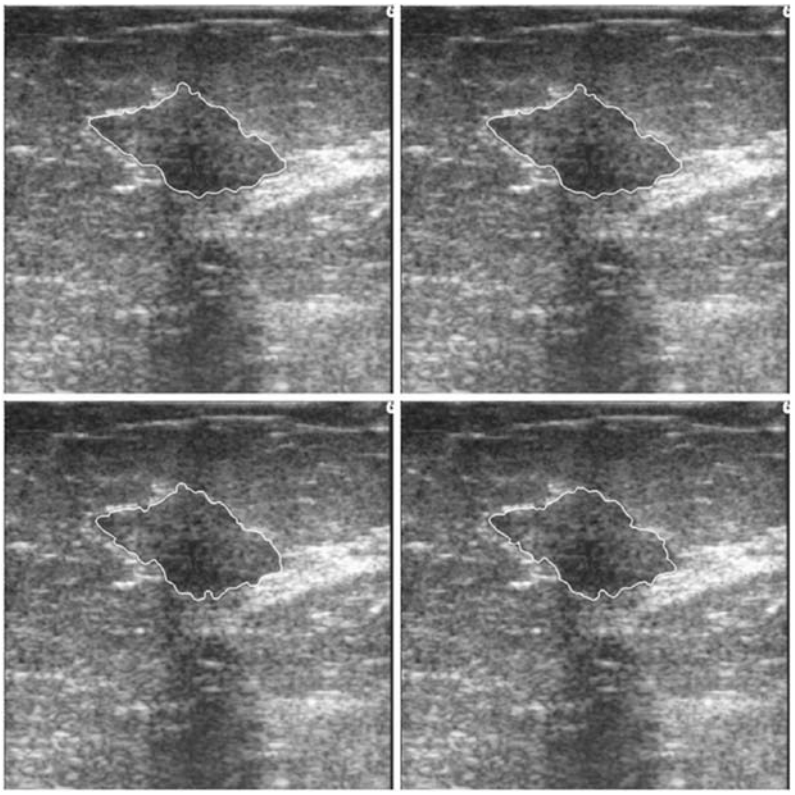

Fig. 11 Comparison of the use of the median or the mean and the variance of the responses of the Gabor filters as region descriptors to improve the location of the edges of the nodules. From left to right and top to bottom: local median, local mean + variance, global median and global mean + variance

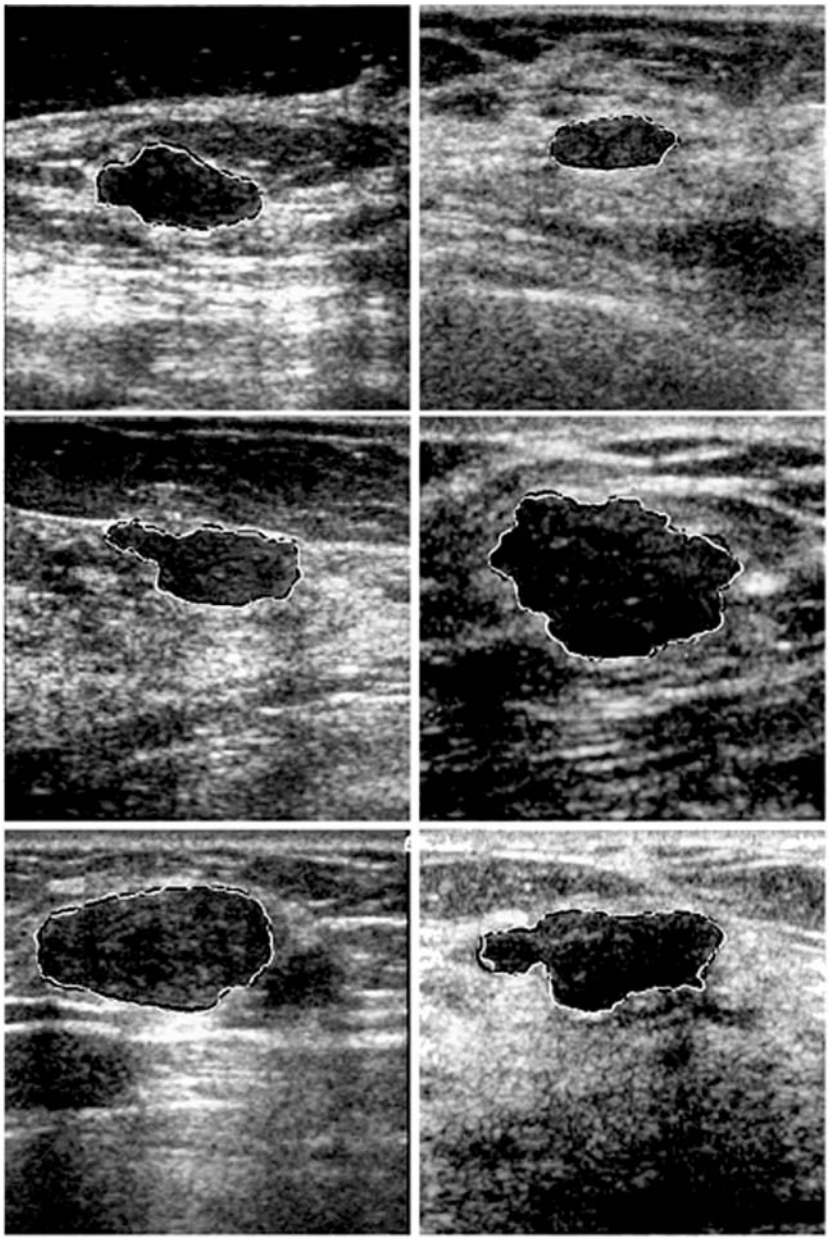

Fig. 12 Comparison of the final segmentations computed using (40) (white) and the reference segmentations obtained from the manually delineated contours performed by the specialists (black)

In order to test the accuracy of our results in a large set of nodules, we have used a set of manually delineated segmentations. We consider a segmentation as the set of 2D points inside a segmentation curve. Two specialists have segmented 32 images. Each nodule has been segmented twice by each specialist in an independent way, i.e., in different days and without considering the first segmentation when performing the second one, so that 4 manual segmentations are available for each nodule. This allows measuring the intra-observer and inter-observer differences, that is, the difference between the segmentations performed by the same physician as well as the difference between segmentations performed by different physicians.

Furthermore, as we have more than one segmentation to be considered as our ground truth, a reference segmentation was extracted by selecting those points which had been included in more than two of the four manual segmentations. Figure 12 shows some examples of the semi-automatic results and the corresponding reference segmentations. As observed, even if the parameters of the geodesic active contours used for all nodules have been the same, all of them are result in satisfactory segmentations, which proves the robustness of these techniques.

Two measures have been used to perform the comparisons:

The first one is called coincidence percentage (CP), and gives us an idea of what proportion of the segmentations is

Table 3 Results using different semi-automatic approaches: presegmentation, geodesic active contours, geodesic active contours with Gabor-based texture information and the manual segmentations performed by the physicians are compared with the reference segmentation. The mean, median and standard deviation for coincidence percentage (CP, see (42)) and proportional distance (PD, see (43)) are shown

	CP			PD		
	Median	Mean	SD	Median	Mean	SD
Presegmentation	83.454	81.615	9.83	6.86	7.85	4.61
Geodesic Active Contours	89.983	87.935	6.93	4.30	5.09	3.08
GAC + Texture	90.445	88.317	6.76	4.24	4.96	2.96
Physicians	94.022	92.897	4.55	2.36	2.91	1.93

Table 4 Intra-observer, inter-observer and system results. In order to compute the intra-observer values, we calculate the mean of the values of CP and PD when comparing, first, the two segmentations of the first physician, and then, the two segmentations of the second physician. Inter-observer values are the mean of the comparisons of the segmentations performed by different physicians. The system-physicians values are the mean of the comparisons of the system's results with all the manual segmentations. The mean, median ans standard deviation for coincidence percentage (CP, see (42)) and proportional distance (PD, see (43)) are shown

	CP			PD		
	Median	Mean	SD	Median	Mean	SD
Intra-observer	90.706	89.660	4.30	3.86	4.27	1.75
Inter-observer	89.229	87.774	5.85	4.51	5.12	2.52
System-Physicians	88.849	86.118	8.44	4.95	6.05	4.06

coincident. This is given by the number of pixels in the intersection of both segmentations with respect to the number of pixels in their union. This is a very intuitive measure, but does not provide any information about how far the differing regions are. Thus, a pixel which is in one of the segmentations and not in the other one, but is very close to it contributes as much as one that is very far from the other segmentation. Let S_1 and S_2 be two segmentations that we wish to compare, the percentage of coincidence between both is given by:

$$\mathrm{CP}(S_1, S_2) = \frac{|S_1 \cap S_2|}{|S_1 \cup S_2|} * 100. \tag{42}$$

The second measure, called proportional distance (PD), tries to measure, not only if there are differing pixels, but also how far they are. First, we calculate the mean distance from the pixels in the contour of one of the segmentations to the contour of the other one, and vice versa. The mean of both measures provides an idea of how far both contours are. However, this is measured in pixels, so that the size of the nodule and the resolution of the images could affect the results. That is the reason why we divide it by the square root of the area of the reference segmentation, so that the distance is expressed with respect to the size of the nodule. To be able to express it in a more intuitive way, we introduce the factor $1/\sqrt{\pi}$, since this would be the ratio between the radius and the square root of the area if the nodule were circular. This way, the proportional distance reflects what proportion of the radius of the circle with the same area represents the distance between both contours. Let S_1 and S_2 be two segmentations that we wish to compare, let C_1 and C_2 be their respective contours, and let RS be the reference segmentation, the proportional distance between both is given by:

$$\mathrm{PD}(S_1, S_2) = \frac{\frac{\sum_{x_i \in C_1} d(x_i, C_2)}{|C_1|} + \frac{\sum_{x_i \in C_2} d(x_i, C_1)}{|C_2|}}{2\sqrt{\frac{|\mathrm{RS}|}{\pi}}} * 100, \tag{43}$$

where $d(x, C)$ is the distance from the point x to the contour C. As shown, the first measure determines the similarity between both segmentations, whereas the second one describes the dissimilarity. Consequently, the higher the first and the lower the second, the more similar the segmentations are.

Table 3 shows a comparison between the reference segmentation and three semi-automatic segmentations for the 32 nodules. Then mean and median of the 32 results are shown using both measures. The first one is the presegmentation, the second one is the segmentation using geodesic active contours (20) and the third one is the segmentation using geodesic active regions with texture information (see (40)). As observed, the use of GAC provides a significant improvement with respect to the initial presegmentation. Furthermore, the use of texture information improves even more the already good results of the GAC. The last row allows comparing the results for the semiautomatic segmentations with those for the manual segmentations. Of course, as the reference segmentation has been

extracted from the manual segmentations, the differences from the latter to the reference one are very small, providing a measure of the dispersion of the manual results.

Table 4 shows a comparison of the intra-observer and inter-observer difference with the difference between the semi-automatic segmentation and all manual segmentations. As expected, the intra-observer differences are lower than the intra-observer ones and those are less than the semi-automatic ones. However, even though the results of the semi-automatic segmentation are not as good as the manual ones, the differences are small, and we could consider them as quite satisfactory.

6 Conclusion

We have presented a new approach in the segmentation of breast tumors in ultrasound images. We use known techniques, such as anisotropic diffusion, balloon methods, Gabor filters or geodesic active contours. The combination of such techniques, taking advantage of the benefits of each one, as well as the introduction of certain texture descriptors for a better filtering, pre-segmentation and final segmentation provide quite satisfactory results in the case of very complex data, such as ultrasound images. First, the proposed anisotropic texture-guided diffusion generates a very suitable image for the initial segmentation, since diffusion is performed across the regions which present similar texture features and inhibited when a change in the descriptors is found. By means of a set of Gabor filters with different scales, orientations and frequencies, we obtain a texture-based region description which allows measuring the similarity between two patterns. The distance in these responses is used to enhance or inhibit the diffusion.

Secondly, the use of the proposed front propagation scheme of balloon type, in which gradient information is used to control the speed of the propagation, produces more robust initial segmentations. Even if there is no suitable threshold to identify a closed contour for the nodule, the possible gaps that may appear do not produce a drastic overflow in the growing process.

Finally, the use of region information in the evolution of the snakes allows a more accurate location of the edges of the tumors. The introduction of texture information in terms of Gabor filter response allows a more complete description of the regions and, therefore, a more precise location of their boundaries [34]. The fact that we search for equidistant inner and outer medians, instead of a high gradient in the edge description, allows locating the edges when they are blurred, non-uniform or gradual. The numerical experiments are quite promising. The final segmentation obtained after all proposed phases are very competitive with respect to the manual segmentation of the nodules performed by the specialists.

Although these models have been developed for the particular case of ultrasound images, they could also be applied to any other type of images. However, the characteristic speckle noise of these images and the precision necessary for the study of the benign and malignant findings require a deep texture analysis which could be simplified in other applications in which textures are more clearly identified. Thus, the same scheme could be used in many practical applications for which classical methods do not provide satisfactory results.

Acknowledgements The authors would like to thank Patricia Alemán-Flores, Rafael Fuentes-Pavón and José Manuel Santana-Montesdeoca, for providing the medical background, the manual segmentations and the suggestions to this work, as well as the Hospital Universitario Insular de Gran Canaria for the ultrasonographic images. The third author acknowledges partial support by the Departament d'Universitats, Recerca i Societat de la Informació de la Generalitat de Catalunya and by PNPGC project, reference BFM2003-02125. We would like to thank Nir Sochen for pointing out his work to us. The first and second authors acknowledge the support of the Ministerio de Educación y Ciencia, reference TIN2005-02004.

Appendix 1 Level Set Formulation of Geometric Curve Evolution

Let us briefly recall the implicit level set formulation of the curve evolution equation

$$C_t = \gamma \mathbf{n}, \tag{44}$$

where $C(t, \tilde{s})$ is an evolving curve in $\mathbb{R}^2$, t represents the time parameter of the evolution, $\tilde{s}$ is a parameterization of C, $\mathbf{n}$ is the outer unit normal to the curve C and γ is the speed of evolution of the curve which is a function of x (i.e., the position of the curve) and the geometric quantities $\mathbf{n}$ and the curvature κ of C. We assume that the curve $C(t)$ is a level set of an evolving function $u(t, x, y)$, $(x, y) \in \mathbb{R}^2$. To fix ideas, let us assume that $C(t)$ is the zero level set of $u(t, x, y)$, and $u(t, x, y)$ is positive inside the zero level-set, and negative outside (in some cases, the signed distance function is a preferred choice). Thus, we have

$$u(t, C(t)) = 0.$$

Differentiating the above identity with respect to t we obtain

$$u_t + \langle \nabla u, C_t \rangle = 0.$$

Using the relation $\mathbf{n} = -\nabla u / \|\nabla u\|$, we have

$$\begin{aligned} u_t &= -\langle \nabla u, C_t \rangle = -\langle \nabla u, \gamma \mathbf{n} \rangle \\ &= \gamma \left\langle \nabla u, \frac{\nabla u}{\|\nabla u\|} \right\rangle = \gamma \|\nabla u\|. \end{aligned}$$

This derivation was the basis of the level set formulation of geometric curve evolutions and can be found in [29].

Appendix 2 Numerical Implementation of Active Contours

Geodesic active contours require a close initialization to reach the desired contour. Otherwise, the contour would tend to round and reduce. Many applications ask the user to manually introduce a set a several dozens of points to build a polygon which will be used as initial contour. Since we apply a front propagation algorithm before the snakes, the pre-segmentation obtained with this technique is used as initial contour C_{init}. Then we define u_0 by assigning the signed distance to the contour C_{init} to every point (one could also simply define a function with two different values inside and outside C_{init}). Then the level set formulation of geodesic active contours is used to make the contour evolve. To discretize (20) we use the explicit discretization scheme obtained by adapting the standard scheme proposed in [29], which we simply write as:

$$\frac{u_{i,j}^{n+1}-u_{i,j}^{n}}{\tau}=g_\sigma(I_{ij}^n)\operatorname{div}\left(\frac{\nabla u_{ij}^n}{\|\nabla u_{ij}^n\|}\right)\|\nabla u_{ij}^n\| + \lambda\nabla u_{ij}^n\cdot\nabla g_\sigma(I_{ij}^n), \tag{45}$$

where $\tau>0$.

To obtain $g_\sigma(I_{ij}^n)$, we first use an approximation of the Gaussian filter, based on the heat equation [1], then we estimate the gradient, and then calculate

$$g_\sigma(I_{ij})=\frac{1}{\sqrt{1+\alpha\|\nabla(I_\sigma)_{ij}\|^2}}.$$

For the estimation of the gradients, we use the masks described in (8).

As explained in Sect. 4, we use a multiscale implementation, starting with higher values of σ for the initialization provided by the pre-segmentation, and reducing it at each scale. Given a final standard deviation σ_0 and a number of scales $\widehat{S}$, the standard deviations used at the different scales are $\widehat{S}\sigma_0, (\widehat{S}-1)\sigma_0, \ldots, \sigma_0$.

In the case of the vectorial descriptor, we compute the set of Gabor filters by convolving with the corresponding kernels. From the outputs of these filters, we extract the corresponding median values (or mean values when we tested this case) and compute the term $M_{G,\text{app}}$ defined in (39). To discretize (38) with $M_{G,\text{app}}$ in place of M_G we adapt again the standard scheme in [29] and we write:

$$\begin{aligned}&\frac{u_{i,j}^{n+1}-u_{i,j}^{n}}{\tau}\\&=g_\sigma(I_{ij}^n)\operatorname{div}\left(\frac{\nabla u_{ij}^n}{\|\nabla u_{ij}^n\|}\right)\|\nabla u_{ij}^n\|\\&\quad+\lambda\nabla u_{ij}^n\cdot\nabla g_\sigma(I_{ij}^n)+\|\nabla u^n\|M_{G,app}(I^n,u^n),\end{aligned}$$

where $\tau>0$. We also use the same type of scheme to discretize (40).

References

1. Álvarez, L., Mazorra, L.: Signal and image restoration using shock filter and anisotropic diffusion. SIAM J. Numer. Anal. **31**(2), 590–605 (1994)
2. Brox, T., Weickert, J.: Level set based image segmentation with multiple regions. In: Pattern Recognition. Lecture Notes in Computer Science, vol. 3175, pp. 415–423 (2004)
3. Brox, T., Weickert, J., Burgeth, B., Mrázek, P.: Nonlinear structure tensors. Image Vis. Comput. **24**(1), 41–55 (2006)
4. Caselles, V., Catté, F., Coll, T., Dibos, F.: A geometric model for active contours in image processing. Numer. Math. **66**, 1–31 (1993)
5. Caselles, V., Kimmel, R., Sapiro, G.: Geodesic active contours. In: Proc. of Fifth International Conference on Computer Vision, pp. 694–699 (1995)
6. Caselles, V., Kimmel, R., Sapiro, G.: Geodesic active contours. Int. J. Comput. Vis. **22**(1), 61–79 (1997)
7. Caselles, V., Kimmel, R., Sapiro, G.: Geometric active contours for image segmentation. In: Bovik, A. (ed.) Handbook of Video and Image Processing, 2nd edn., pp. 613–627 (2005)
8. Chan, T.F., Sandberg, B.Y., Vese, L.A.: Active contours without edges for vector-valued images. J. Vis. Commun. Image Represent. **11**(2), 130–141 (2000)
9. Chan, T., Vese, L.: An active contour model without edges. In: Scale-Space Theory in Computer Vision. Lecture Notes in Computer Science, vol. 1682, pp. 141–151 (1999)
10. Chan, T.F., Vese, L.A.: Active contours and segmentation models using geometric pde's for medical imaging. In: Malladi, R. (ed.) Geometric Methods in Bio-Medical Image Processing, Series: Mathematics and Visualization, pp. 63–75. Springer, Berlin (2002)
11. Chen, D.R., Chang, R.F., Juang, Y.L.: Computer-aided diagnosis applied to us of solid breast nodules by using neural networks. Radiology **213**, 407–412 (1999)
12. Cheng, C.M., Chou, Y.H., Han, K.C., Hung, G.S., Tiu, C.M., Chiou, H.J., Chiou, S.Y.: Breast lesions on sonograms: Computer-aided diagnosis with nearly setting-independent features and artificial neural networks. Radiology **226**, 504–514 (2003)
13. Cohen, L.D.: On active contour models and balloons. Comput. Vis. Graph. Image Process. **53**(2), 211–218 (1991)
14. Cremers, D., Soatto, S.: Motion Competition: A variational framework for piecewise parametric motion segmentation. Int. J. Comput. Vis. **62**(3), 249–265 (2005)
15. Cremers, D., Tischhäuser, F., Weickert, J., Schnörr, C.: Diffusion snakes: introducing statistical shape knowledge into the Mumford-Shah functional. Int. J. Comput. Vis. **50**, 295–313 (2002)
16. Davis, E.R.: On the noise suppression and image enhancement characteristics of the median, truncated median and mode filters. Pattern Recognit. Lett. **7**, 87–97 (1988)
17. Frost, V.S., Stiles, J.A., Shanmugan, K.S., Holtzman, J.C.: A model for radar images and its application to adaptive digital filtering of multiplicative noise. IEEE Trans. Pattern Anal. Mach. Intell. **4**, 157–165 (1982)
18. Gabor, D.: Theory of communications. J. IEEE **93**, 429–459 (1946)
19. Heiler, M., Schnörr, C.: Natural image statistics for natural image. Int. J. Comput. Vis. **63**(1), 5–19 (2005)
20. Hernandez, M., Frangi, A.F.: Geodesic active regions using non-parametric statistical regional description and their application to aneurysm segmentation from CTA. LNCS **3150**, 94–102 (2004)

21. Kass, M., Witkin, A., Terzopoulos, D.: Snakes: Active contour models. In: 1st International Conference on Computer Vision, pp. 259–268 (1987)
22. Kaufhold, J., Chan, R., Karl, W.C., Castanon, D.A.: Ultrasound tissue analysis and characterization. In: Proc. of SPIE, pp. 73–83 (1999)
23. Kichenassamy, S., Kumar, A., Olver, P., Tannenbaum, A., Yezzi, A.: Conformal curvature flows: from phase transitions to active vision. Arch. Ration. Mech. Anal. **134**(3), 275–301 (1996)
24. Kimmel, R., Bruckstein, A.M.: On regularized Laplacian zero crossings and other optimal edge integrators. Int. J. Comput. Vis. **53**, 225–243 (2003)
25. Kuan, D.T., Sawchuck, A.A., Strand, T.C., Chavel, P.: Adaptive noise smoothing filter for images with signal-dependent noise. IEEE Trans. Pattern Anal. Mach. Intell. **7**, 165–177 (1985)
26. Kuo, W.J., Chang, R.F., Moon, W.K., Lee, C.C., Chen, D.R.: Computeraided diagnosis of breast tumors with different us systems. Acad. Radiol. **9**, 793–799 (2002)
27. Lee, J.S.: Digital image enhancement and noise filtering by use of local statistics. IEEE Trans. Pattern Anal. Mach. Intell. **2**(2), 165–168 (1980)
28. Malladi, R., Sethian, J.A., Vemuri, B.C.: Shape modeling with front propagation: a level set approach. IEEE Trans. Pattern Anal. Mach. Intell. **17**, 158–175 (1995)
29. Osher, S., Sethian, J.: Fronts propagating with curvature dependent speed: algorithms based on the Hamilton-Jacobi formulation. J. Comput. Phys. **79**, 12–49 (1988)
30. Paragios, N., Deriche, R.: Geodesic active regions for supervised texture segmentation. In: Proc. of International Conference on Computer Vision (1999)
31. Perona, P., Malik, J.: Scale space and edge detection using anisotropic diffusion. IEEE Trans. Pattern Anal. Mach. Intell. **12**, 629–639 (1990)
32. Rousson, M., Brox, T., Deriche, R.: Active unsupervised texture segmentation on a diffusion based feature space. In: IEEE Conference on Computer Vision and Pattern Recognition (CVPR), pp. 699–704 (2003)
33. Rousson, M., Cremers, D.: Efficient kernel density estimation of shape and intensity priors for level set segmentation. In: Gerig, G. (ed.) Medical Image Comput. and Comp.-Ass. Interv. (MICCAI). LNCS Springer, vol. 3750, pp. 757–764 (2005)
34. Sagiv, C., Sochen, N.: Integrated active contours for texture segmentation. IEEE Trans. Image Process. **1**(1), 415–423 (2004)
35. Sandberg, B., Chan, T., Vese, L.: A level-set and Gabor-based active contour algorithm for segmenting textured images. Technical Report 39, Math. Dept. UCLA, Los Angeles, USA, July 2002
36. Stavros, A.T., Thickman, D., Rapp, C.L., Dennis, M.A., Parker, S.H., Sisney, G.A.: Solid breast nodules: Use of sonography to distinguish between benign and malignant lesions. Radiology **196**(1), 123–134 (1995)
37. Weickert, J.: Anisotropic diffusion in image processing. In: ECMI Series, Teubner, Stuttgart (1998)
38. Yu, Y., Acton, S.T.: Speckle reducing anisotropic diffusion. IEEE Trans. Image Process. **11**(11), 1260–1270 (2003)

Miguel Alemán-Flores B.S. in Computer Science (1995) and Ph.D. in Computer Science (2002) from the University of Las Palmas de Gran Canaria, Spain, is a lecturer at the Department of Computer Science of this university. His main research interests include image processing, computer vision and medical imaging.

Luis Álvarez received a M.Sc. in applied mathematics in 1985 and a Ph.D. in mathematics in 1988, both from Complutense University (Madrid, Spain). Between 1991 and 1992 he worked as post-doctoral researcher at CEREMADE, Université Paris IX (Dauphine) (France). Currently he is with the Departamento de Informatica y Sistemas of Universidad de Las Palmas de Gran Canaria. His main research interest area is the application of the mathematical analysis to computer vision.

Vicent Caselles received the Licenciatura and Ph.D. degrees in mathematics from Valencia University, Spain, in 1982 and 1985, respectively. Currently, he is professor at the Pompeu Fabra University (Barcelona). He is an associate member of IEEE. His research interests include image processing, computer vision, and the applications of geometry and partial differential equations to both previous fields.